Check for updates

RESEARCH ARTICLE

ADVANCED MATERIALS INTERFACES
www.advmatinterfaces.de

Efficient Combination of Surface Texturing and Functional Coating for Very Low Secondary Electron Yield Surfaces and Rough Nonevaporable Getter Films

Marcel Himmerlich, Danilo A. Zanin, Mauro Taborelli, Angelo Rafael Granadeiro Costa, Pedro Costa Pinto, Lucia Lain Amador, Wilhelmus Vollenberg, Adrienn Baris, Elisa Garcia-Tabares Valdivieso, Ana Teresa Perez Fontenla, Stefan Wackerow, and Amin Abdolvand*

The formation of a fissured copper surface by picosecond pulsed laser irradiation is combined with functional coatings consisting of Ti and amorphous carbon layers or a Ti–Zr–V compound film to fabricate surfaces with the maximum of the secondary electron yield being as low as 0.4. By structural and spectroscopic analysis of the formed surfaces it is demonstrated that both coatings enclose the nanostructures generated by redeposition of metal structures from the laser-induced plasma plume, keeping the initial topography intact. This allows an efficient elimination of secondary electron emission by combining the benefits from structural surface modification and adaption of electronic surface properties to efficiently dissipate the energy of impinging electrons. Thermal activation tests of the Ti–Zr–V nonevaporable getter films revealed that for films on nanostructured substrates, which have a much higher effective surface, a slight diminution of surface activation occurs at 160 and 200 °C, while this effect is completely compensated when heating up to 250 °C indicating promising pumping capabilities. Both examples highlight the benefits from combining 3D substrate patterning with classical 2D deposition technologies.

1. Introduction

The electron-induced emission of electrons is often quantified by the secondary electron yield (SEY), sometimes also referred to as total electron yield (TEY). Low SEY materials or surfaces are aimed for reduction of surface charging of spacecrafts and satellites[1,2] as well as to mitigate formation of electron clouds in particle accelerators.[3–7] The primary electron energy dependence of the secondary electron yield as well as the kinetic energy distribution of the emitted electrons are subject of intensive studies since decades for elemental material surfaces and compounds[7–17] to accommodate the progressively developing technology demands. For many applications a SEY maximum below unity is sufficient to avoid cascade multiplication of the impinging electrons. However, for other solutions it could be beneficial to reduce the SEY even further in order to suppress reflected, backscattered, and secondary electrons that could potentially generate background noise or deteriorate the measured signal, as for example in electron collectors, for the measurement of low electron currents in ultra-high vacuum (UHV) or for ionization based pressure gauges.[18,19]

The material parameters that influence the electron yield are numerous. Since the emitted electrons are generated in a depth of a few nanometers, it is determined by the properties of the near-surface region of the material, such as the degree of oxidation of a metal,[20] the existence of adsorbates or surface impurities, or in general the surface chemical composition.[21,22] In consequence, deposition of functional thin films can be used to influence the SEY[23,24] and especially amorphous carbon coatings and titanium nitride (TiN) are nowadays utilized for particle accelerator components.[6,25–28] In addition, surface modification processes after installation in vacuum, such as thermal treatments[29] or electron irradiation,[30–34] have an effect on the electron emission properties. For vacuum components of particle accelerators that can be heated to temperatures above 180 °C, the implementation of nonevaporable getter (NEG) films to mitigate electron cloud is one possible

M. Himmerlich, D. A. Zanin, M. Taborelli, A. R. Granadeiro Costa, P. Costa Pinto, L. Lain Amador, W. Vollenberg, A. Baris, E. Garcia-Tabares Valdivieso, A. T. Perez Fontenla
CERN
European Organization for Nuclear Research
Meyrin 1211, Switzerland
E-mail: marcel.himmerlich@cern.ch

E. Garcia-Tabares Valdivieso
Departamento de Física
Universidad Carlos III de Madrid
Madrid, Spain

S. Wackerow, A. Abdolvand
School of Science & Engineering
University of Dundee
Scotland, UK

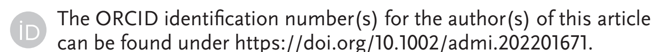
The ORCID identification number(s) for the author(s) of this article can be found under https://doi.org/10.1002/admi.202201671.

© 2022 The Authors. Advanced Materials Interfaces published by Wiley-VCH GmbH. This is an open access article under the terms of the Creative Commons Attribution License, which permits use, distribution and reproduction in any medium, provided the original work is properly cited.

DOI: 10.1002/admi.202201671

© 2022 The Authors. Advanced Materials Interfaces published by Wiley-VCH GmbH

21967350, 2023, 1, Downloaded from https://onlinelibrary.wiley.com/doi/10.1002/admi.202201671 by Cern, Wiley Online Library on [25/01/2023]. See the Terms and Conditions (https://onlinelibrary.wiley.com/terms-and-conditions) on Wiley Online Library for rules of use; OA articles are governed by the applicable Creative Commons License

approach. It has been adopted for the straight sections of the Large Hadron Collider (LHC).[35] Indeed, after thermal activation, NEG layers not only exhibit a high vacuum pumping capacity,[36] but also a low SEY.[29,37,38]

Another approach for electron emission reduction is the roughening or texturing of the material surface on different length scales, which allows to trap and reabsorb emitted electrons in cavities at the surface. A SEY reduction can be obtained by surface roughening,[39–43] machining of deep trenches or grooves,[44–47] and several approaches to create a micro- or nanostructured morphology. Microporous structures[48–50] as well as a sponge or foam topology[51–54] enable trapping of impinging and emitted electrons as efficiently as textured surfaces formed by etching[55] or nanowires created by different techniques.[56–59] Furthermore, plasma-based nanostructure formation[60] as well as laser-induced surface structuring on different length scales[61–64] have been validated to reduce secondary electron emission.

As the various surface structuring technologies also modify the surface composition, both influencing factors have to be considered in parallel, while their quantitative contributions to SEY changes are often difficult to disentangle. A combination of the effect of surface structuring and modification of the chemical composition by thin film deposition to obtain surfaces with low SEY was already reported for TiN layers on grooved substrates[38] as well as Ti and Ti–Pd films on laser-structured copper surfaces,[65] while depositing Ti–V–Hf–Zr films onto laser-structured Al did not reduce the SEY.[66] Furthermore, annealing of laser-induced CuO nanoparticles on Cu in UHV lead to the chemical reduction of the surface to Cu_2O, which induced a significant SEY decrease.[67]

In this study we follow the approach to compare two types of representative thin film coatings for accelerator vacuum technology (a-C/Ti and Ti–Zr–V) on flat and nanostructured substrates to characterize the individual contributions of surface roughening and material surface composition on electron emissivity. The aim of the work is to explore the possibility to obtain surfaces with very low SEY by combining artificial roughness with coatings of materials that intrinsically exhibit a low SEY. In order to disentangle the two contributions, we characterized coatings of sufficient thickness assuring that all emitted secondary electrons originate from the top layer only and that no electron emission from the substrate underneath occurs. For non-insulating materials, this condition is satisfied if the film thickness exceeds 20–30 nm.[68–70]

2. Results and Discussion

Top-view scanning electron micrographs at three magnifications of different laser/structured samples (from left to right: solely laser-treated, laser-treatment + a-C/Ti coating, laser-treatment + Ti–Zr–V coating) are shown in **Figure 1**. The laser-treated surface exhibits the typical trench pattern covered by nanoparticles[61,63] that originate from redeposition of material from the generated plasma plume. Most importantly, the two coatings, a-C/Ti layers or Ti–Zr–V NEG films, do not significantly modify the surface topography on micrometer scale—they homogeneously enclose the nanostructures. To further characterize the geometric features of the surface, we have prepared cross-sectional side views by a focused ion beam (FIB) system. **Figure 2** includes selected micrographs in the sample top regions with the nanoparticle generated by the laser processing and the top layers created by physical vapour deposition for the a-C coating (top) and the Ti–Zr–V (bottom) coatings. The different layers on top of the fissured nanoparticles, as indicated by different arrows, were identified by energy disperse X-ray spectroscopy (EDX) mapping (see Supporting Information). As the plasma-deposition processes are not isotropic, local variations of the film thickness are evident. However, the top of the nanostructures surface is homogeneously covered by either layers of a-C/Ti or a Ti–V–Zr film. For the a-C and Ti layers, the nominal thicknesses compared to coatings on flat substrates were not obtained: the thickness of the a-C layer is in the range of a few nanometers up to 35 nm, while the Ti sublayer is up to 110 nm thick. The average layer thicknesses of a flat Cu reference sample, that was coated during the same run, were 185 nm for the layer Ti and 86 nm for the topmost a-C layer. Consequently, the layers deposited on the nanostructures of the laser-treated Cu samples are thinner. We attribute this difference to the special geometry of the coating setup with its cylindrical target and radial geometry as well as to the larger effective surface to be coated by the same amount of ablated target material and possible projection and shadowing effects on the rough surface. On the other hand, the NEG alloy thickness is close to the nominal value of 1.5 µm as on flat reference substrates, as they had been deposited in a magnetron system with planar target. The top view and cross-sectional electron micrographs clearly show that the dendritic fine structure of the particles top side, that faces the ion flux during coating, is covered by the different deposited layers, while the particulate-induced surface topography is maintained. Therefore, the individual particle topography is changed after coating, leading to smoothing of the surface on the nanometer scale.

As the SEY is dependent on both, the surface topography as well as the chemical and electronic material properties, we have furthermore characterized these surfaces by X-ray photoelectron spectroscopy (XPS). **Figure 3** includes selected XPS survey spectra of the laser-treated Cu surface before and after a-C/Ti coating or NEG coating, respectively. The surface properties of degreased Cu OFE and Cu after laser-treatment in N_2 are discussed in detail in refs. [34] and [67], respectively. For both coatings, the spectra of films deposited on flat Cu substrates (not shown) are almost identical to the ones on the laser-roughened Cu (Figure 3). After a-C coating, only signals related to oxygen and carbon are detected. This is typical for an a-C surface after exposure to air[28] and proves that a compact layer free of pores or cracks was deposited, since neither a Cu substrate nor a Ti interlayer signal is detected. For the NEG coating, Ti, V, and Zr signals are detected as well as oxygen and carbon, which originate from oxidation of the film in air and adsorption of ambient residual molecules. A slight substrate-related Cu2p signal is detected for the NEG film on the laser-treated rough Cu, while such feature is absent for the film on flat Cu. Consequently, the film can be considered sufficiently pure since it is free of surface impurities.

The thermal activation of the NEG films modifies their surface composition.[29,71] The variation of the main metal components as well as the C and O signals were monitored during the

© 2022 The Authors. Advanced Materials Interfaces published by Wiley-VCH GmbH

21967350, 2023, 1, Downloaded from https://onlinelibrary.wiley.com/doi/10.1002/admi.202201671 by Cern, Wiley Online Library on [25/01/2023]. See the Terms and Conditions (https://onlinelibrary.wiley.com/terms-and-conditions) on Wiley Online Library for rules of use; OA articles are governed by the applicable Creative Commons License

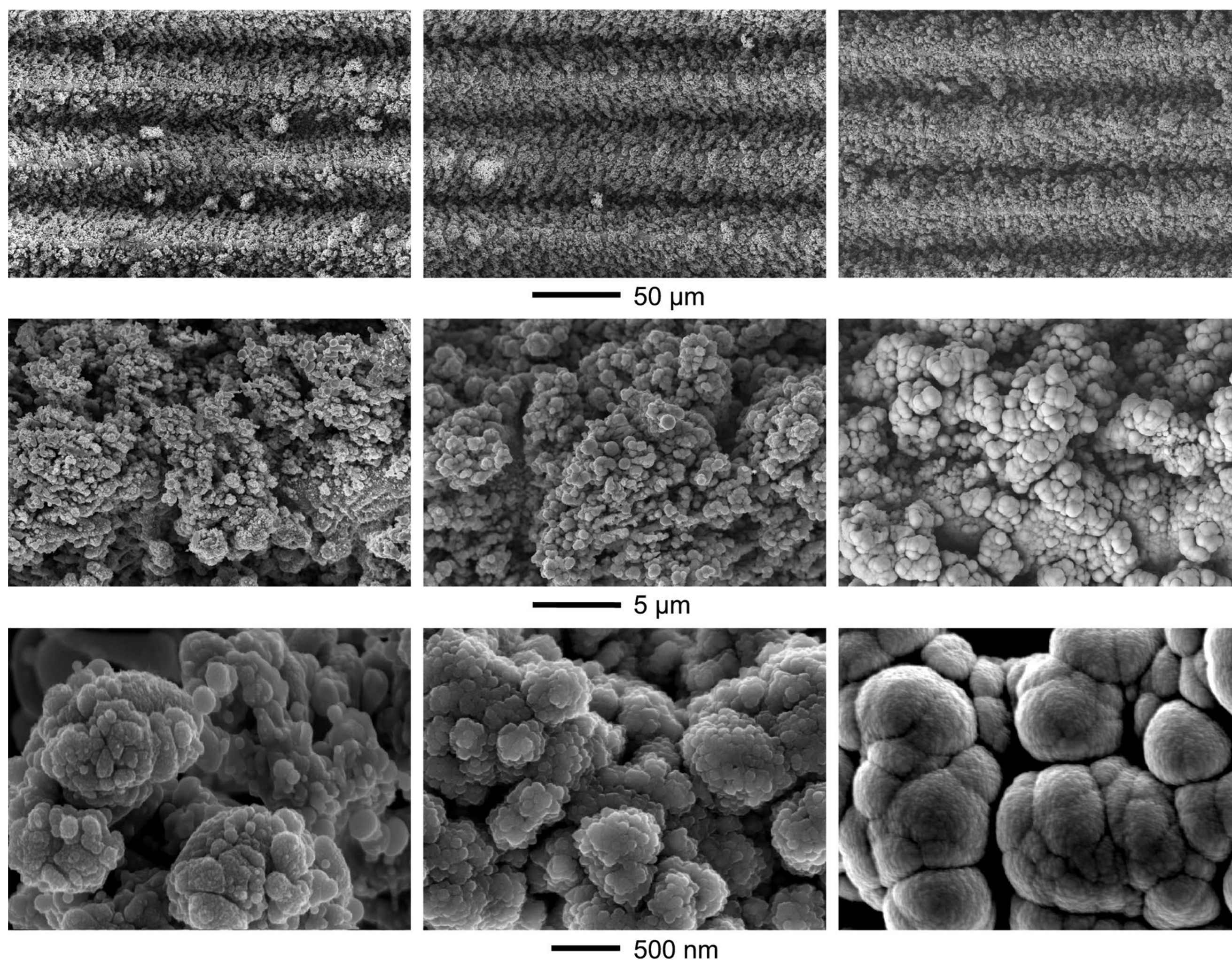

Figure 1. Top-view secondary electron micrographs at three different magnifications (from top to bottom) for the laser-treated Cu surface (left), after additional a-C/Ti coating (center), or additional Ti–Zr–V NEG coating (right).

activation sequence of annealing the sample at 160, 200, and 250 °C for 1 h each. The change in XPS core level spectra is documented in **Figure 4**. The shift of the V2p, Ti2p, Zr3d states to lower binding energy is characteristic for the chemical reduction of the metal elements and a loss of surface metal–oxygen bonds,[72,73] which is traceable by the reduction of the O1s signal intensity (see Figure 4c,f). Furthermore, the states in the C1s spectra shift from ≈285 to ≈282.5 eV above 200 °C, induced by a transformation of hydrocarbon adsorbates on the reactive surface and formation of metal carbide bonds.[72,74] The comparison of the activation behavior for the NEG films on flat and laser-structured substrate reveals the same trends in surface transformation. At 160 and 200 °C, the chemical reduction of the rough sample is slightly delayed compared to the flat layer. This could be linked to the 3D nature of the NEG-coated structures. The effective oxidized surface area as well as the surface-to-volume-ratio are larger, possibly limiting film deoxidation. Furthermore the surfaces of the redeposited nanoparticles might not reach the same temperature for the given heating power due to lower thermal conductivity through the nanoparticles and a higher emissivity of the rough surface.[75] However, annealing at 250 °C leads to a consistent degree of surface activation. This result is interesting since the higher effective surface area of rough films potentially allows a higher pumping speed and adsorption capacity as getter material if properly activated.[36]

The primary electron energy (E_p) dependence of the SEY ($\delta(E_p)$) for the different samples is plotted in **Figure 5**, where (a) includes the curves for degreased flat Cu and laser-treated Cu with and without a-C/Ti coating, while (b) compares $\delta(E_p)$ of NEG films on flat and laser-treated Cu prior and after thermal activation at 250 °C in UHV. Clear differences are observed and all three approaches (a-C coating, laser-roughening and thermal NEG activation in UHV) induce significant SEY reductions. To quantitatively illustrate the trends, the SEY maxima δ_{max} for each sample together with the related primary electron energy $E_p(\delta_{max})$ are summarized in **Table 1**.

The a-C coating reduces the SEY maximum of flat Cu (≈2.2) to 0.94. This coating strategy to reduce the SEY of materials was already successfully applied for in-situ coatings in the super-proton-synchrotron[76] and the Large Hadron Collider at CERN. The laser-structured Cu sample exhibits a δ_{max} of 0.86, comparable to earlier reported values of identically

© 2022 The Authors. Advanced Materials Interfaces published by Wiley-VCH GmbH

21967350, 2023, 1, Downloaded from https://onlinelibrary.wiley.com/doi/10.1002/admi.202201671 by Cern, Wiley Online Library on [25/01/2023]. See the Terms and Conditions (https://onlinelibrary.wiley.com/terms-and-conditions) on Wiley Online Library for rules of use; OA articles are governed by the applicable Creative Commons License

ADVANCED MATERIALS INTERFACES
www.advmatinterfaces.de

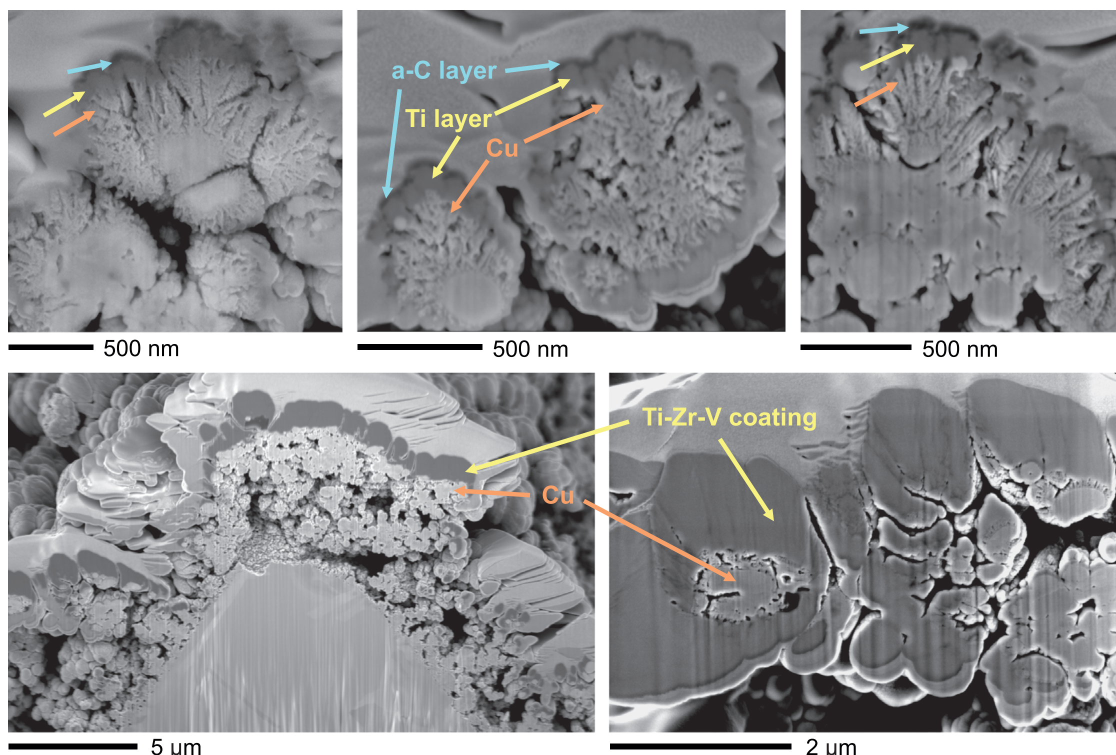

Figure 2. Selected cross-section scanning electron micrographs at different spots of a a-C/Ti coating on laser-treated Cu (top) and a Ti–Zr–V NEG coating on laser-treated Cu (bottom). The bright top regions correspond to the Pt coating used for protecting the surface during FIB milling and is not indicated by arrows in the figures.

prepared samples.[63] For laser-structured samples with additional a-C surface layer, the SEY has a maximum of only 0.4 at $E_p = 300$ eV. It is important to note that, although the a-C layer thickness in this case is only 35 nm, all emitted secondary electrons originate solely from the top coating, while any emission of electrons from the nanostructured substrate underneath can be neglected due to the short electron mean free path. When analyzing the shape of $\delta(E_p)$ for the two a-C coated samples in Figure 5a, the nature of the a-C coating defines the energetic maximum at around 300 eV. The carbon top layer induces a reduction of δ_{max} by a factor α_{comp} of 2.3 and 2.2 for the flat and the rough substrate, respectively. Consequently, as the analyses revealed that the surface topography/roughness is maintained after coating and since the chemical composition of the layers on rough and flat substrate are identical, these numbers prove the additive benefit of combining surface roughening and deposition of proper layers for lowering the SEY. On the other hand, the improvement when comparing coated rough to flat surfaces corresponds to a factor α_{struc} of 2.3. One should consider the slight differences in the general SEY curve shape, which is due to the different materials that the electrons interact with as well as due to the nanostructured surface in case of laser treatment. Obviously, shifts of $E_p(\delta_{max})$ are not reflected in this simplified quantification. The laser roughening shifts $E_p(\delta_{max})$ to higher energy[63,67,77] compared to a flat surface of the same composition. The a-C/Ti coating on that rough template certainly induces a shift of $E_p(\delta_{max})$ back to smaller energy, but the tendency of a higher relative SEY at $E_p > E_p(\delta_{max})$ remains, which is due to the surface roughness. Consequently, a unified scaling factor of the SEY curve across the whole energy range does not exist.

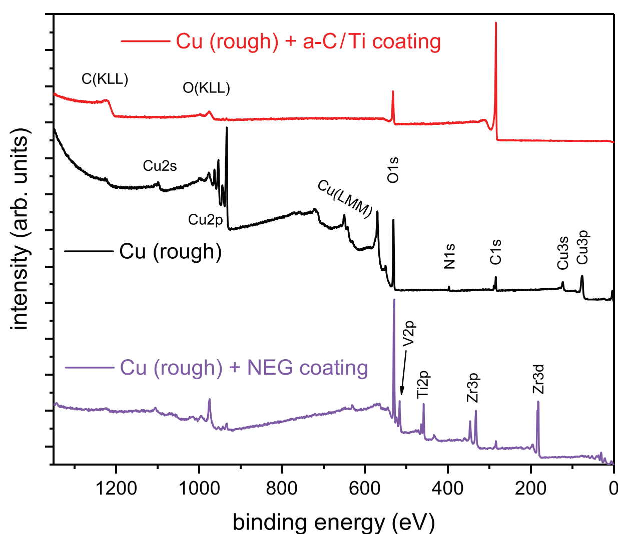

Figure 3. XPS survey spectra of the laser-treated Cu sample without (black) and with additional a-C/Ti (red) or Ti–Zr–V NEG (purple) coating.

The same trend is found for the surfaces that had been coated by the NEG layer. In this case, the additional experimental possibility to modify the composition of the outermost surface via a thermal treatment in UHV, allows to get an even better quantitative picture. The improvement of the SEY before

© 2022 The Authors. Advanced Materials Interfaces published by Wiley-VCH GmbH

21967350, 2023, 1, Downloaded from https://onlinelibrary.wiley.com/doi/10.1002/admi.202201671 by Cern, Wiley Online Library on [25/01/2023]. See the Terms and Conditions (https://onlinelibrary.wiley.com/terms-and-conditions) on Wiley Online Library for rules of use; OA articles are governed by the applicable Creative Commons License

ADVANCED SCIENCE NEWS
www.advancedsciencenews.com

ADVANCED MATERIALS INTERFACES
www.advmatinterfaces.de

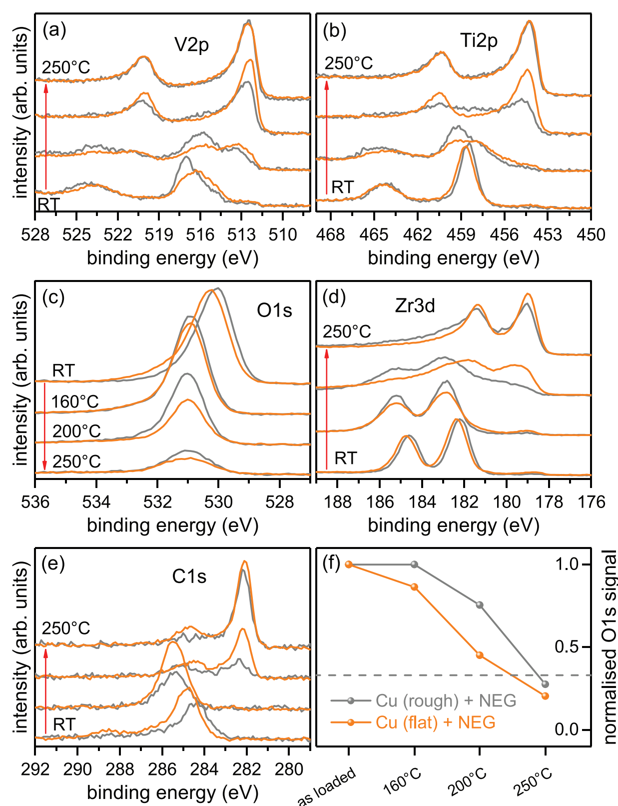

Figure 4. XPS analysis of the thermal activation processing of the Ti–Zr–V coatings on flat Cu (orange) and the laser-treated Cu (gray). a–e) V2p, Ti2p, O1s, Zr3d, and C1s core level spectra. f) Intensity variation of the normalized O1s signal. The dashed line in (f) represents a mark for an intensity reduction by 66.6% as quantitative threshold for effective NEG film activation.

and after activation corresponds to a reduction factor α_{comp} of 1.8 and 1.7 for the flat and rough sample, respectively. The SEY reduction relies on several factors and is directly linked to the composition of the NEG film, that is, a) the degree of oxidation and the amount of surface impurities of the initial

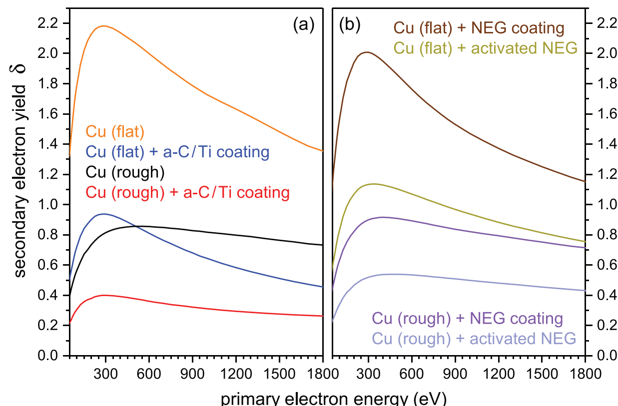

Figure 5. Secondary electron yield in dependence of primary electron energy between 50 and 1800 eV for a) flat and laser-treated (rough) copper samples with and without additional a-C/Ti coating and b) Ti–Zr–V NEG coatings on flat and laser-treated (rough) copper samples before and after thermal activation at 250 °C in UHV.

Table 1. Summary of SEY maximum δ_{max} and its energy $E_p(\delta_{max})$ for all characterized samples on laser-treated (rough) and untreated (flat) Cu samples.

Sample	δ_{max}	$E_p(\delta_{max})$
Cu (flat)	2.18	300 eV
Cu (flat) + a-C/Ti coating	0.94	275 eV
Cu (rough)	0.86	500 eV
Cu (rough) + a-C/Ti	0.40	300 eV
Cu (flat) + NEG coating	2.01	300 eV
Cu (flat) + NEG–activated	1.14	325 eV
Cu (rough) + NEG coating	0.92	400 eV
Cu (rough) + NEG–activated	0.54	500 eV

NEG surface, which depends on sample storage conditions, and b) the temperature and vacuum conditions during the activation process as well as its duration, which define the degree of film deoxidation and adsorbate modification.[37] For example for activation of a Ti–Zr–V film at 210 °C for 2 h, a factor α_{comp} of 1.5[38] was found, while in a different study an improvement factor of 1.9 was reported after activation at up to 300 °C for 2 h.[37] For V-rich Ti–Zr–V films that had been initially activated at 450 °C after growth, then exposed to air and finally annealed for a long period of 24 h at 200 °C, α_{comp} varied between 1.9 and 2.1 in dependence of film growth conditions.[29]

These α_{comp} values account for the improvement ratio due to changes in the material surface composition and the related electron-interaction characteristics, while the factor α_{struc} comparing flat versus rough NEG surfaces is in both studied cases (as received NEG and after thermal activation) 2.2, which is in agreement with the topography-related reduction factor of the a-C films. One has to keep in mind that this contribution is very dependent on the actual surface roughness or topographical changes, while the compositional contribution is believed to be constant for the same material. For example, the structural SEY reduction factor α_{struc} of grooved compared to flat surfaces was reported to be 1.9 for bare aluminum samples and 1.8 if an additional TiN top layer was added.[38]

These two examples show that when preserving the general sample topography after coating, the two approaches for SEY reduction, namely i) surface structuring to enhance the scattering of impinging primary electrons and generated secondaries, which hinders their emission to vacuum, and ii) coating the surface with a material that has an intrinsic low SEY (its structural and electronic properties allow an efficient impact electron energy dissipation) and is chemically inert, or modifying the surface composition by other means such as thermally induced deoxidation/desorption or electron-induced surface conditioning. In the presented cases the individual reduction factors α_i combine: $\delta_{max,final} = \alpha_{struc}^{-1} \cdot \alpha_{comp}^{-1} \cdot \delta_{max,initial}$.

3. Conclusion

The microscale topography of laser-structured copper is preserved when coated by thin films using magnetron sputtering. The two concepts for electron multipacting mitigation, a)

© 2022 The Authors. Advanced Materials Interfaces published by Wiley-VCH GmbH

21967350, 2023, 1, Downloaded from https://onlinelibrary.wiley.com/doi/10.1002/admi.202201671 by Cern, Wiley Online Library on [25/01/2023]. See the Terms and Conditions (https://onlinelibrary.wiley.com/terms-and-conditions) on Wiley Online Library for rules of use; OA articles are governed by the applicable Creative Commons License

21967350, 2023, 1, Downloaded from https://onlinelibrary.wiley.com/doi/10.1002/admi.202201671 by Cern, Wiley Online Library on [25/01/2023]. See the Terms and Conditions (https://onlinelibrary.wiley.com/terms-and-conditions) on Wiley Online Library for rules of use; OA articles are governed by the applicable Creative Commons License

surface structuring and b) coating with a low-SEY material, can be combined. The two contributions appear to multiply their individual effects allowing a SEY maximum of 0.4 for a-C/Ti layers and 0.54 for Ti–Zr–V films after thermal activation on laser-structured copper. Furthermore, Ti–Zr–V nonevaporable getter films deposited onto the laser-structured metal are efficiently activated when heated in UHV to 250 °C. Considering their high effective surface area, it is anticipated that fabrication of rough NEG films on prestructured substrates could be an interesting strategy for high pumping speed and adsorption capacity. As for all nanostructures, the abrasion resistance of the Cu surfaces after laser processing is inferior to that of a bulk solid material. For applications where mechanical impact might be expected, this aspect should be considered for enduring performance of the functional top layers, may it be for SEY reduction, for active pumping elements or others. Considering possible applications in particle accelerators, further studies have to explore the influence of the processing on the impedance of the surfaces. Nonetheless, the results demonstrate that the combination of prestructuring of metal substrates by a laser-treatment and deposition of a thin film enable improved functionality of the active surface, which is linked to the larger effective surface area as well as to the enhancement of the tailored properties of the functional top layer when deposited onto a nanostructured template.

4. Experimental Section

Polycrystalline copper OFE (oxygen-free electronic grade) metal sheets of 1 mm thickness were cut into pieces of size between 1×1 and 2×2 cm^2 and subsequently underwent a standard procedure for UHV cleaning including a wet-chemical detergent-based degreasing process followed by rinsing in deionized water. Laser-engineered surface structuring of Cu OFE was realized using a 10 ps pulsed 532 nm laser operated at a repetition rate of 200 kHz as described in detail in ref. [63] The laser was operated at maximum power and the beam was attenuated remotely such that a focused (4σ spot diameter of 52 µm) average fluence of ≈0.9 J cm^{-2} (peak fluence of 1.9 J cm^{-2}) was incident upon the copper surface, corresponding to an equivalent average power of 4 W. The surface was modified by raster-scanning the sample with respect to the laser spot using a speed of 15 mm s^{-1} and a distance 45 µm between individual lines, creating parallel grooves that were decorated by nanoparticles. A laminar flow of nitrogen was directed toward the interaction zone to reduce surface oxidation.

Samples were coated with amorphous carbon using a modular magnetron sputtering source, which was equipped with two cylindrical targets (99.95% titanium and 99.92% graphite). The two targets can be polarized independently and the magnetic field was provided by small cylindrical permanent magnets (length and diameter 8 mm), sealed inside a cylindrical stainless-steel case. The total length of the titanium and graphite target was 12 and 24 cm, respectively. To deploy the coating, the sputtering source moved inside the assembly via pulling by two stainless steel cables. The samples were placed at a target-substrate distance of 11.4 mm. The coating was deployed in a two-step procedure. The base pressure in the system was $<2 \times 10^{-7}$ mbar and argon with a purity of 99.9999% was used as discharge gas. First, a titanium sublayer with a nominal thickness of ≈100 nm was directly applied at 2.5×10^{-2} mbar Ar pressure. In a second step performed at 1×10^{-1} mbar Ar and 20 W without exposing the first coating to air, ≈100–150 nm of Ti were added followed by deposition of a nominally 80–100 nm thick a-C layer on top of the titanium. During the deposition of the carbon, the titanium target was intermittently operated in order to provide a fresh getter surface near the area where the carbon layer was being deposited to locally reduce the partial pressure of hydrogen. A low amount of incorporated impurities was a prerequisite for low SEY amorphous carbon films.[27]

NEG films were deposited onto cleaned flat CuOFE samples as well as the laser-patterned Cu samples via DC sputtering using a 150 mm diameter magnetron. An alloyed disc cathode made of titanium, zirconium, and vanadium with a nominal atomic composition of 1:1:1 from NEYCO was used as target to sputter ≈1.5 µm of Ti–Zr–V at an average power of 320 W using krypton as discharge gas. The samples were mounted at a distance of 200 mm from the cathode. Prior to the coating, the system was baked for 20 h at 135 °C with the samples being already inserted to obtain a base pressure of $<1 \times 10^{-7}$ mbar after letting it cool down to room temperature. The deposition was performed for 3 h at a Kr pressure of 8×10^{-4} mbar. The film composition and thickness of the NEG coatings were measured afterward by X-ray fluorescence. The layer on the flat Cu substrates had a composition of $Ti_{0.34}Zr_{0.33}V_{0.33}$ and a thickness of (1.36 ± 0.03) µm, while the NEG composition and thickness on the laser-structured samples were $Ti_{0.40}Zr_{0.32}V_{0.28}$ and (1.45 ± 0.04) µm, respectively.

After finalization of the coating, the samples were exposed to the laboratory air and directly wrapped in aluminum foil for storage prior insertion (within a period of 1–2 days) to the UHV surface analysis system with a base pressure of $< 2 \times 10^{-10}$ mbar. The SEY – δ, defined as the ratio between the numbers of emitted electrons and impinging electrons, was measured with an ELG-2 electron gun (Kimball Physics, Inc., Wilton, USA) by the method of alternating sample bias[34] ($V_{sa} = \pm 47.1$ V) using an electron current of ≈2 nA focused to a spot diameter of 1 mm. The sample current was measured using an optical isolation amplifier with a gain of 10^8 V A^{-1} and a 6517B electrometer (Keithley Instruments, Inc., Cleveland, USA). The estimated dose associated with a single SEY measurement was $\approx 2 \times 10^{-7}$ C mm^{-2}. The reproducibility of the measurement was estimated from the acquisition of two consecutive SEY curves at the same sample position to 0.01 on the maximum SEY. The SEY measurements were performed prior to XPS analysis to avoid any X-ray-induced conditioning effect of the surface, which could impact the SEY values. NEG thermal activation cycles were performed via heating of the sample holder backside by a resistive filament heater in the UHV chamber. The NEG activation test cycles consisted of three heating steps: a) heating from room temperature to 160 °C at a rate of 5 K min^{-1} and keeping the temperature for 1 h, b) heating from 160 to 200 °C (5 K min^{-1}) and keeping the temperature for 1 h, and c) heating from 200 to 250 °C (5 K min^{-1}) and keeping the temperature for 1 h. The sample temperature was measured by a thermocouple attached to the system manipulator in close proximity to the sample. The setup had beforehand been calibrated with a second thermocouple placed in the position of the mounted NEG samples and by comparing to the melting temperature of an indium sample. The surface chemical composition was characterized by X-ray photoelectron spectroscopy using a hemispherical electron energy analyzer with nine channeltrons (Phoibos 150, SPECS Surface Nano Analysis GmbH, Berlin, Germany) and a monochromated AlKα X-ray source (XR 50M, $h\nu$ = 1486.7 eV). The XPS measurements during the NEG activation cycles were performed at the respective annealing temperature without cool-down to room temperature.

Field emission scanning electron microscopy was employed to characterize the specimens surface. A ZEISS Sigma system with InLens secondary electron detector was utilized. In order to determine the film thickness and the formed surface topography, a FIB system in dual beam configuration with scanning electron microscopy (Crossbeam 540 from ZEISS, Ga^+ source) was used to prepare cross-sectional views. First, a 10×5 µm^2 platinum barrier of 2 µm thickness was deposited on top of the area of interest (300 pA current and 30 kV acceleration voltage) in order to facilitate effective polishing. FIB milling was then performed in subsequent steps at 700 and 300 pA at an acceleration voltage of 30 keV to create a smooth surface that could be effectively imaged. All images were acquired using an InLens secondary electron detector at low acceleration voltage (3–5 keV) for optimum image contrast. EDX mapping was additionally performed to identify the composition of the layers unambiguously. EDX data

© 2022 The Authors. Advanced Materials Interfaces published by Wiley-VCH GmbH

were collected on the cross-sections at 10 kV acceleration voltage and a dwell time of 300 µs per pixel using an Oxford Instruments 50 mm^2 X-max silicon drift detector. The evaluation was performed using version 3.3 of the AZtec software.

Supporting Information

Supporting Information is available from the Wiley Online Library or from the author.

Acknowledgements

The authors would like to acknowledge the support from the Science & Technology Facilities Council (STFC) of the United Kingdom (Grant No. ST/T001887/1). L.L.A. is grateful for the support by the CERN Knowledge Transfer fund.

Conflict of Interest

The authors declare no conflict of interest.

Data Availability Statement

The data that support the findings of this study are available from the corresponding author upon reasonable request.

Keywords

amorphous carbon, laser roughening, nanostructured functional coatings, nonevaporable getters, secondary electron yield reduction

Received: August 22, 2022
Published online: November 6, 2022

[1] N. Balcon, D. Payan, M. Belhaj, T. Tondu, V. Inguimbert, *IEEE Trans. Plasma Sci.* **2012**, *40*, 282.
[2] S. T. Lai, *IEEE Trans. Plasma Sci.* **2013**, *41*, 3492.
[3] M. Izawa, Y. Sato, T. Toyomasu, *Phys. Rev. Lett.* **1995**, *74*, 5044.
[4] W. Fischer, M. Blaskiewicz, J. M. Brennan, H. Huang, H.-C. Hseuh, V. Ptitsyn, T. Roser, P. Thieberger, D. Trbojevic, J. Wei, S. Y. Zhang, U. Iriso, *Phys. Rev. Accel. Beams* **2008**, *11*, 041002.
[5] O. Domínguez, K. Li, G. Arduini, E. Métral, G. Rumolo, F. Zimmermann, H. M. Cuna, *Phys. Rev. Accel. Beams* **2013**, *16*, 011003.
[6] Y. Suetsugu, K. Shibata, T. Ishibashi, K. Kanazawa, M. Shirai, S. Terui, H. Hisamatsu, *Phys. Rev. Accel. Beams* **2016**, *19*, 121001.
[7] R. Cimino, T. Demma, *Int. J. Mod. Phys. A* **2014**, *29*, 1430023.
[8] R. Warnecke, *J. Phys. Radium* **1936**, *7*, 270.
[9] H. Bruining, J. H. De Boer, *Physica* **1938**, *5*, 17.
[10] R. Kollath, in Springer, Berlin, Heidelberg **1956**, pp. 232–303.
[11] K. Kanaya, S. Ono, F. Ishigaki, *J. Phys. D Appl. Phys.* **1978**, *11*, 2425.
[12] Z. J. Ding, X. D. Tang, R. Shimizu, *J. Appl. Phys.* **2001**, *89*, 718.
[13] Y. Lin, D. C. Joy, *Surf. Interface Anal.* **2005**, *37*, 895.
[14] C. G. H. Walker, M. M. El-Gomati, A. M. D. Assa'd, M. Zadražil, *Scanning* **2008**, *30*, 365.
[15] A. K. F. Haque, M. M. Haque, M. A. R. Patoary, M. A. Uddin, M. I. Hossain, M. S. Mahbub, A. K. Basak, M. Maaza, B. C. Saha, *Vacuum* **2017**, *141*, 192.
[16] R. Cimino, I. R. Collins, M. A. Furman, M. Pivi, F. Ruggiero, G. Rumolo, F. Zimmermann, *Phys. Rev. Lett.* **2004**, *93*, 014801.
[17] S. Schulte, G. Hartung, J. Kröger, M. Himmerlich, V. Petit, M. Taborelli, *Phys. Rev. Accel. Beams* **2020**, *23*, 103101.
[18] I. Figueiredo, N. Bundaleski, O. Teodoro, K. Jousten, C. Illgen, *Vacuum* **2021**, *184*, 109907.
[19] B. Jenninger, J. Anderson, M. Bernien, N. Bundaleski, H. Dimitrova, M. Granovskij, C. Illgen, J. Setina, K. Jousten, P. Kucharski, C. Reinhardt, F. Scuderi, R. A. S. Silva, A. Stöltzel, O. M. N. D. Teodoro, B. Trzpil-Jurgielewicz, M. Wüest, *Vacuum* **2021**, *183*, 109884.
[20] I. Bojko, N. Hilleret, C. Scheuerlein, *J. Vac. Sci. Technol. A* **2000**, *18*, 972.
[21] P. Riccardi, M. Pisarra, A. Cupolillo, M. Commisso, A. Sindona, R. A. Baragiola, C. A. Dukes, *J. Phys. Condens. Matter* **2010**, *22*, 305004.
[22] A. Kuzucan, H. Neupert, M. Taborelli, H. Störi, *J. Vac. Sci. Technol. A* **2012**, *30*, 051401.
[23] H. Wolff, *Ann. Phys.* **1941**, *431*, 591.
[24] F. Wang, Q. Zhao, J. Li, K. Wang, Z. Huang, W. Cui, *Coatings* **2018**, *8*, 249.
[25] D. Ruzic, R. Moore, D. Manos, S. Cohen, *J. Vac. Sci. Technol.* **1982**, *20*, 1313.
[26] C. Yin Vallgren, G. Arduini, J. Bauche, S. Calatroni, P. Chiggiato, K. Cornelis, P. C. Pinto, B. Henrist, E. Métral, H. Neupert, G. Rumolo, E. Shaposhnikova, M. Taborelli, *Phys. Rev. Accel. Beams* **2011**, *14*, 071001.
[27] P. Costa Pinto, S. Calatroni, H. Neupert, D. Letant-Delrieux, P. Edwards, P. Chiggiato, M. Taborelli, W. Vollenberg, C. Yin-Vallgren, J. L. Colaux, S. Lucas, *Vacuum* **2013**, *98*, 29.
[28] H. Moreno Fernández, M. Himmerlich, P. Costa Pinto, J. Coroa, D. Sousa, A. Baris, M. Taborelli, *Appl. Surf. Sci.* **2021**, *542*, 148552.
[29] M. Nishiwaki, S. Kato, *J. Vac. Sci. Technol. A* **2007**, *25*, 675.
[30] M. Nishiwaki, S. Kato, *Appl. Surf. Sci.* **2001**, *169-170*, 700.
[31] B. Henrist, N. Hilleret, C. Scheuerlein, M. Taborelli, G. Vorlaufer, in *Proc. 8th Eur. Particle Accelerator Conf. (EPAC)*, European Physical Society Interdivisional Group on Accelerators, Mulhouse **2002**, pp. 2553–2555.
[32] C. Scheuerlein, M. Taborelli, N. Hilleret, A. Brown, M. A. Baker, *Appl. Surf. Sci.* **2002**, *202*, 57.
[33] R. Cimino, M. Commisso, D. R. Grosso, T. Demma, V. Baglin, R. Flammini, R. Larciprete, *Phys. Rev. Lett.* **2012**, *109*, 064801.
[34] V. Petit, M. Taborelli, H. Neupert, P. Chiggiato, M. Belhaj, *Phys. Rev. Accel. Beams* **2019**, *22*, 083101.
[35] P. Chiggiato, P. Costa Pinto, *Thin Solid Films* **2006**, *515*, 382.
[36] C. Benvenuti, P. Chiggiato, P. Costa Pinto, A. Escudeiro Santana, T. Hedley, A. Mongelluzzo, V. Ruzinov, I. Wevers, *Vacuum* **2001**, *60*, 57.
[37] B. Henrist, N. Hilleret, C. Scheuerlein, M. Taborelli, *Appl. Surf. Sci.* **2001**, *172*, 95.
[38] F. Le Pimpec, R. Kirby, F. King, M. Pivi, *Nucl. Instrum. Methods A* **2005**, *551*, 187.
[39] M. Kussmaul, M. J. Mirtich, A. Curren, *Surf. Coat. Technol.* **1992**, *51*, 299.
[40] M. Cao, N. Zhang, T.-C. Hu, F. Wang, W.-Z. Cui, *J. Phys. D Appl. Phys.* **2015**, *48*, 055501.
[41] N. Zhang, M. Cao, W.-Z. Cui, T.-C. Hu, *Jap. J. Appl. Phys.* **2017**, *56*, 075802.
[42] M. Ye, P. Feng, Y. Li, D. Wang, Y. He, W. Cui, *J. Appl. Phys.* **2019**, *125*, 043301.
[43] I. Montero, L. Olano, L. Aguilera, M. E. Dávila, U. Wochner, D. Raboso, P. Martín-Iglesias, *J. Electron Spectrosc.* **2020**, *241*, 146822.
[44] L. Wang, K. Bane, C. Chen, T. Himel, M. Munro, M. Pivi, T. Raubenheimer, G. Stupakov, in *Proc. IEEE Particle Accelerator Conf. (PAC)*, IEEE, Piscataway, NJ **2007**, pp. 4234–4236.

© 2022 The Authors. Advanced Materials Interfaces published by Wiley-VCH GmbH

21967350, 2023, 1, Downloaded from https://onlinelibrary.wiley.com/doi/10.1002/admi.202201671 by Cern, Wiley Online Library on [25/01/2023]. See the Terms and Conditions (https://onlinelibrary.wiley.com/terms-and-conditions) on Wiley Online Library for rules of use; OA articles are governed by the applicable Creative Commons License

ADVANCED MATERIALS INTERFACES
www.advmatinterfaces.de

[45] M. Pivi, F. K. King, R. E. Kirby, T. O. Raubenheimer, G. Stupakov, F. Le Pimpec, *J. Appl. Phys.* **2008**, *104*, 104904.
[46] Y. Suetsugu, H. Fukuma, K. Shibata, M. Pivi, L. Wang, in *Proc. Int. Particle Accelerator Conf. (IPAC)*, JACoW, Geneva **2010**, pp. 2021–2023.
[47] J. Pierron, C. Inguimbert, M. Belhaj, J. Puech, M. Raine, *J. Appl. Phys.* **2018**, *124*, 095101.
[48] M. Ye, Y. N. He, S. G. Hu, R. Wang, T. C. Hu, J. Yang, W. Z. Cui, *J. Appl. Phys.* **2013**, *113*, 074904.
[49] J. M. Sattler, R. A. Coutu, R. Lake, T. Laurvick, T. Back, S. Fairchild, *J. Appl. Phys.* **2017**, *122*, 055304.
[50] J. Ludwick, A. Iqbal, D. Gortat, J. D. Cook, M. Cahay, P. Zhang, T. C. Back, S. Fairchild, M. Sparkes, W. O'Neill, *J. Vac. Sci. Technol. B* **2020**, *38*, 054001.
[51] R. Cimino, A. Romano, S. Petracca, A. Stabile, M. R. Masullo, S. O'Connor, G. Bregliozzi, V. Baglin, in *Proc. Int. Particle Accelerator Conf. (IPAC)*, JACoW, Geneva **2014**, p. WEPME033.
[52] C. Swanson, I. D. Kaganovich, *J. Appl. Phys.* **2018**, *123*, 023302.
[53] A. Alvarado, H.-Y. Chang, W. Nadvornick, N. Ghoniem, J. Marian, *Appl. Surf. Sci.* **2019**, *478*, 142.
[54] D. Dickstein, H.-Y. Chang, J. Marian, M. Feldman, A. Hubble, R. Spektor, N. Ghoniem, *J. Appl. Phys.* **2020**, *128*, 123302.
[55] V. Baglin, Yu. Bozhko, O. Grobner, B. Henrist, N. Hilleret, C. Scheuerlein, M. Taborelli, in *Proc. 7th Eur. Particle Accelerator Conf. (EPAC)*, CERN, Geneva **2000**, pp. 217–221.
[56] L. Aguilera, I. Montero, M. E. Dávila, A. Ruiz, L. Galán, V. Nistor, D. Raboso, J. Palomares, F. Soria, *J. Phys. D: Appl. Phys.* **2013**, *46*, 165104.
[57] Y. Raitses, D. Staack, A. Dunaevsky, N. J. Fisch, *J. Appl. Phys.* **2006**, *99*, 036103.
[58] Y. Raitses, I. D. Kaganovich, A. V. Sumant, in *Proc. 33rd Int. Electric Propulsion Conf. (IEPC)*, American Institute of Aeronautics and Astronautics, Washington, D.C. **2013**, pp. IEPC–2013–390.
[59] C. Jin, A. Ottaviano, Y. Raitses, *J. Appl. Phys.* **2017**, *122*, 173301.
[60] M. Patino, Y. Raitses, R. Wirz, *Appl. Phys. Lett.* **2016**, *109*, 201602.
[61] R. Valizadeh, O. B. Malyshev, S. Wang, S. A. Zolotovskaya, W. A. Gillespie, A. Abdolvand, *Appl. Phys. Lett.* **2014**, *105*, 231605.
[62] R. Valizadeh, O. Malyshev, S. Wang, T. Sian, M. Cropper, N. Sykes, *Appl. Surf. Sci.* **2017**, *404*, 370.
[63] D. Bajek, S. Wackerow, D. A. Zanin, L. Baudin, K. Bogdanowicz, E. Garcia-Tabares Valdivieso, S. Calatroni, B. Di Girolamo, M. Sitko, M. Himmerlich, M. Taborelli, P. Chiggiato, A. Abdolvand, *Sci. Rep.* **2020**, *10*, 250.
[64] J. J. J. Nivas, M. Valadan, M. Salvatore, R. Fittipaldi, M. Himmerlich, M. Rimoldi, A. Passarelli, E. Allahyari, S. Oscurato, A. Vecchione, C. Altucci, S. Amoruso, A. Andreone, S. Calatroni, M. R. Masullo, *Surf. Interfaces* **2021**, *25*, 101179.
[65] Y. Gao, S. Wang, J. Wang, Z. You, J. Zhang, Y. Hu, Y. Wu, J. Fan, H. Li, Q. Zhan, H. Yang, Z. Xu, *Materials* **2021**, *14*, 5.
[66] J. Wang, Y. Gao, Z. You, J. Fan, J. Zhang, Z. Qiao, S. Wang, Z. Xu, *Coatings* **2019**, *9*, 12.
[67] S. Calatroni, E. G.-T. Valdivieso, A. T. P. Fontenla, M. Taborelli, H. Neupert, M. Himmerlich, D. Bajek, S. Wackerow, A. Abdolvand, *Phys. Rev. Accel. Beams* **2020**, *23*, 033101.
[68] H. Seiler, *J. Appl. Phys.* **1983**, *54*, R1.
[69] E. Belli, P. C. Pinto, G. Rumolo, A. Sapountzis, T. Sinkovits, M. Taborelli, B. Spataro, M. Zobov, G. Castorina, M. Migliorati, *Phys. Rev. Accel. Beams* **2018**, *21*, 111002.
[70] M. Angelucci, A. Novelli, L. Spallino, A. Liedl, R. Larciprete, R. Cimino, *Phys. Rev. Res.* **2020**, *2*, 032030.
[71] M. P. Lozano, J. Fraxedas, *Surf. Interface Anal.* **2000**, *30*, 623.
[72] K. Masek, F. Sutara, T. Skala, J. Drbohlav, K. Veltruska, V. Matolin, *J. Vac. Sci. Technol. A* **2003**, *21*, 797.
[73] C.-C. Li, J.-L. Huang, R.-J. Lin, D.-F. Lii, C.-H. Chen, *Thin Solid Films* **2007**, *516*, 378.
[74] F. Sutara, T. Skala, K. Masek, V. Matolin, *Vacuum* **2009**, *83*, 824.
[75] S. A. Zolotovskaya, S. Wackerow, H. Neupert, M. J. Barnes, L. V. Cid, B. Teissandier, A. T. Perez Fontenla, A. Abdolvand, *Opt. Mater. Express* **2020**, *10*, 622.
[76] W. Vollenberg, P. Chiggiato, P. C. Pinto, P. Cruikshank, H. Moreno, C. Pasquino, J. P. Espinos, M. Taborelli, in *Proc. 12th Int. Particle Accelerator Conf. (IPAC)*, CERN, Geneva **2021**, p. WEPAB338.
[77] P. Lorenz, M. Himmerlich, M. Ehrhardt, E. Bez, K. Bogdanowicz, M. Taborelli, K. Zimmer, *Lasers Manuf. Mater. Process.* **2022**, *9*, 135.

© 2022 The Authors. Advanced Materials Interfaces published by Wiley-VCH GmbH

21967350, 2023, 1, Downloaded from https://onlinelibrary.wiley.com/doi/10.1002/admi.202201671 by Cern, Wiley Online Library on [25/01/2023]. See the Terms and Conditions (https://onlinelibrary.wiley.com/terms-and-conditions) on Wiley Online Library for rules of use; OA articles are governed by the applicable Creative Commons License